

Quantitative Ultrasonic Characterization of Subsurface Inclusions in Tapered Roller Bearings

Showmic Islam¹, Satyajeet P. Deshpande¹, Luz D. Sotelo¹, Musa Norouzzian¹, Michael T. Lumpkin², Liesl F. Ammerlaan², and Allen J. Fuller², Joseph A. Turner^{1†}

ABSTRACT

Initiation sites for rolling contact fatigue (RCF) in bearing components are often associated with subsurface inclusions. The presence of such defects within the region of maximum shear stress just below the contact surface can increase the local state of stress. Eventually, the high-stress region may initiate microcrack formation, leading to raceway spall that is detrimental to bearing performance. Thus, bearing steel cleanliness is critical, particularly in the near-race region. In this article, recent ultrasonic surface wave inspection methods are described with which subsurface inclusions can be identified and characterized. Our past work has shown that such an approach can be used to identify sub-surface inclusions that spall when subjected to simulated service life tests. Here, the quantitative aspects of this research will be highlighted. The surface wave penetration depth and the reflection amplitude from an inclusion are both frequency dependent. Thus, multi-frequency ultrasonic inspection procedures have been developed to exploit this behavior to identify the size and depth of inclusions. Reference measurements are based on samples created with artificial defects that have a known size and depth. Finite element (FE) modeling is used to identify inclusion sizes and depths that are deemed critical to bearing performance from which the

¹Mechanical and Materials Engineering, W342 Nebraska Hall, University of Nebraska-Lincoln, Lincoln, Nebraska 68588, USA

²Amsted Rail Brenco, 2580 Frontage Road, Petersburg Industrial Park, Petersburg, Virginia 23805, USA

[†] Corresponding author: jaturner@unl.edu

ultrasonic inspection criteria are generated. This work is expected to impact the field of nondestructive testing for bearing components subjected to RCF.

Keywords

rolling contact fatigue, ultrasound inspection, subsurface inclusions, ultrasonic surface waves, bearing spalls

Introduction

Bearings utilized in the freight rail industries must withstand heavy loads. Studies to improve the cleanliness of the steel used for bearing manufacturing are ongoing. A bearing in service has a limited life expectancy due to the potential of subsurface initiated fatigue spalls. Even if a bearing is properly aligned, lubricated, and maintained, it may still fail due to rolling contact fatigue (RCF) [1]-[2]. RCF may result in metallic particles flaking from the surface of the rolling elements or raceways. It often occurs when there are subsurface non-metallic inclusions present in the raceway of bearing components. The subsurface inclusions act as stress concentrators and can serve as crack initiation points [3]. When a crack reaches the raceway surface, metallic debris may be introduced into the bearing, which compromises the bearing performance and may lead to failure. Researchers [4]–[7] have shown that a high level of cleanliness in steel is a factor in minimizing the probability of fatigue spalls in bearings. One study showed that non-metallic inclusions of 40 μm or larger can cause initiations of cracks [4]. Gupta, et al. [8] studied the effect of inclusion type on the level of stress concentration. Their study found that the size, properties and shape of inclusions have a strong effect on the stress concentration value. Guan, et al. [9] further studied the effect of an inclusion on crack formation and found that the location of an inclusion is more important than the inclusion size for crack initiation. Although improvements in the production of steel quality have improved dramatically in recent years, current inspection standards that are

based on optical microscopy do not guarantee that an entire heat of steel is free of inclusions. Typically, inclusions that are closer to the raceway surface are more detrimental than deeper ones. Due to the potential harmful effects of such impurities in bearings, it is essential to develop an inspection system to detect the location and size of inclusions.

Ultrasound is one of the prominent methods used to identify material impurities. Ultrasonic wave propagation in heterogeneous media and flaw detection have been studied to better understand and predict ultrasonic responses [10]–[13]. Although ultrasonic inspection standards exist [14], they are limited in their ability to detect inclusions near the raceway surface. Standard ultrasonic inspections have an inherent blind zone that is a consequence of the pulse width used for the frontwall echo. Thus, near-race inclusions may remain undetected using normal incidence longitudinal waves unless a very high frequency [15] is used, which is expensive and less reliable for industrial use. Ultrasonic surface wave inspection methods have shown promise with respect to the identification of inclusions that ultimately spall [16]–[17]. One complication of this approach is that the wave penetration depth and scattering behavior are both functions of frequency. The amplitude of a surface wave that has reflected from a subsurface inclusion depends on both diameter and depth of the inclusion. Thus, a single frequency cannot differentiate both parameters such that a multi-frequency approach is needed. Measurements at multiple frequencies require careful calibration across the frequencies so that the reflection amplitudes can be compared with one another. In this article, this multi-frequency, surface wave approach is described and applied to the detection of sub-surface inclusions.

Experimental Configuration for Surface Wave Measurements

The use of ultrasonic surface waves has been shown to be effective for detection of near-race inclusions [18], [19]. These types of waves are confined to the sample surface with a depth of

penetration that is on the order of one wavelength [20], [21]. Assuming mechanical properties of steel, the wavelengths for surface waves excited at 7.5, 10, and 15 MHz are approximately 400, 300, and 200 μm , respectively. This range of depth covers the most important zone with respect to subsurface spall initiation [3]. Example measurement results are presented in this section. A schematic of the experimental configuration is shown in FIG. 1(A). The transducer is oriented near the raceway surface above the 2nd critical angle such that the primary waves excited in the sample are surface waves. A focused transducer is used and the focus is placed slightly below the sample surface. During a typical scan, the part (e.g., a bearing outer or inner ring) is rotated 360° and the transducer is translated vertically in the direction parallel to the raceway. As the part is scanned, an ultrasonic pulse is transmitted and the reflected signal is recorded (FIG. 1(B)). The placement of an appropriate gate defines the time window for which the reflections from any inclusions will be detected. The voltage level of the gate defines the threshold, an amplitude selected to identify any inclusions deemed of importance. The image created from such a scan is called a C-scan (FIG. 1(C)).

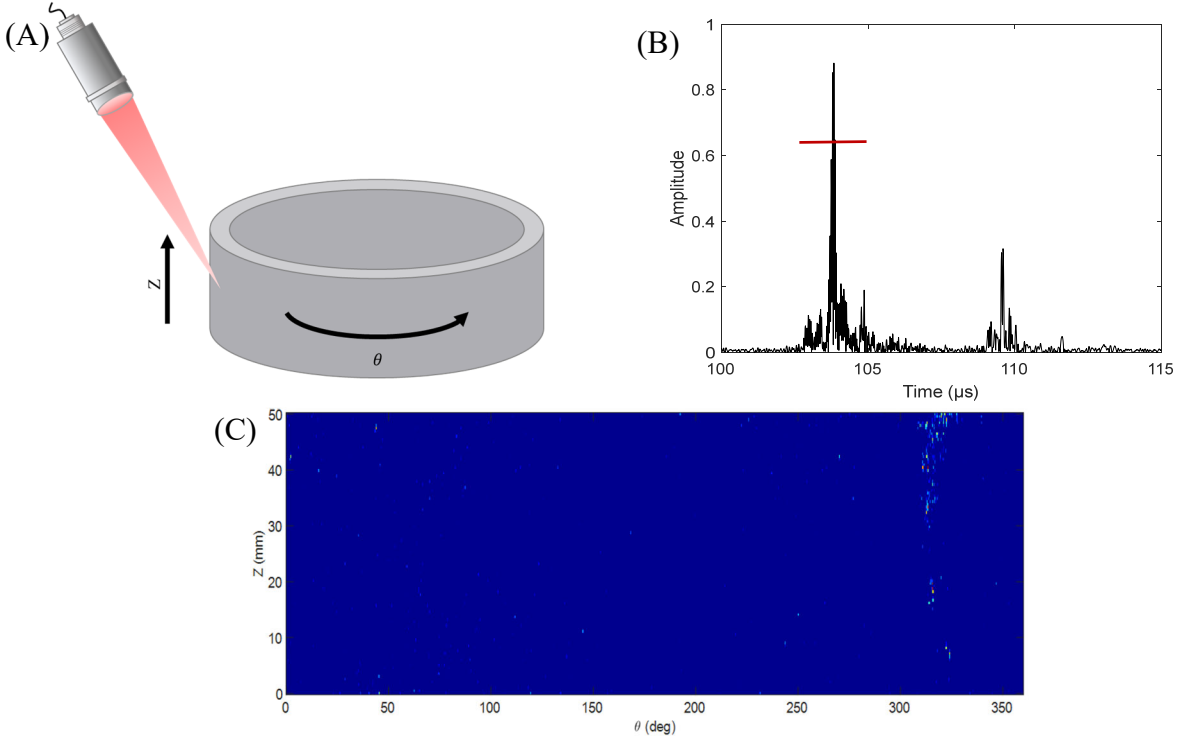


FIG. 1- (A) shows the schematic of the ultrasonic surface wave measurement system. (B) shows the A-scan of one waveform. The red line indicates the location of the gate. The height of the gate is called the gate threshold and (C) shows the resultant C-scan obtained from a collection of the peak amplitudes within the gates of the A-scan for a bearing outer ring.

This approach was used to evaluate bearing outer rings that were manufactured from the same heat of steel. Surface wave C-scans were collected, and the locations of high amplitude reflections were marked. The outer rings were then sectioned, ground, and polished until the inclusions detected

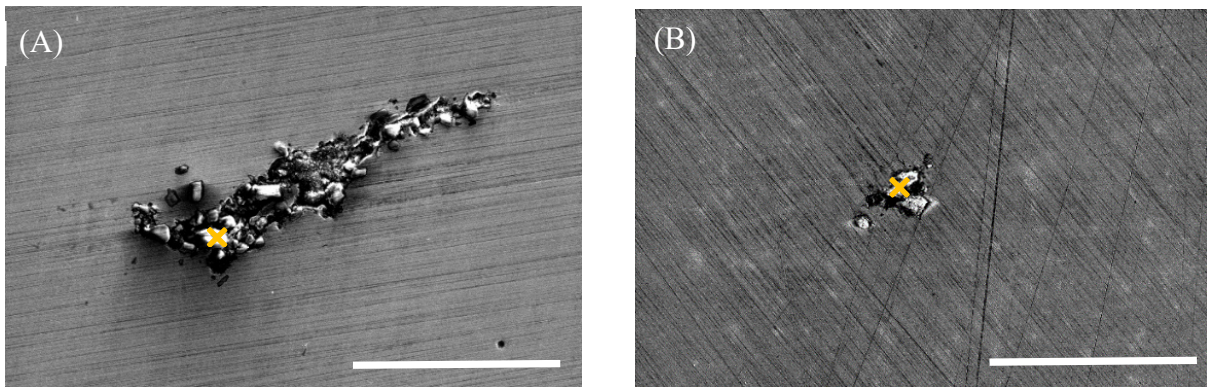


FIG. 2- SEM images showing: (A) a stringer; (B) globular morphologies of two inclusions detected with ultrasonic surface waves. The \times symbol indicates the locations where EDS analysis was performed (scale bars = 50 μm).

with ultrasound were revealed. These inclusions were imaged using scanning electron microscopy (SEM), and their chemical composition was determined using energy dispersive X-ray spectroscopy (EDS). FIG. 2, shows the morphology of two of these inclusions. While some inclusions appear as a string of impurities, or stringers, others have a more globular morphology. Furthermore, the chemical analysis indicates an important presence of aluminum and oxygen in all of the inclusions imaged, as shown in Table 1, suggesting that these inclusions are primarily aluminum oxides. However, traces of other elements were also detected, implying these impurities can have complex chemistry.

Table 1. EDS chemical composition results from the inclusions shown in FIG. 2.

Inclusion A		
Element	Weight %	Atomic %
C	2.97	5.14
O	38.04	49.41
Fe	0.01	0
Al	58.98	45.44
Inclusion B		
Element	Weight %	Atomic %
C	31.61	43.76
O	38.16	39.65
Fe	6.40	1.90
Al	23.83	14.68

Ultrasonic Calibration Methods

Artificial defects such as those created by electrical discharge machining (EDM) or femtosecond laser machining (FLM) were previously used as calibration references [16]. However, the shape and boundary conditions of such manufactured defects are considerably different than those observed in real inclusions in a steel matrix. Thus, a method was developed to create more realistic reference samples. This method uses advanced powder metallurgy techniques to place impurities

of known size and shape at predetermined locations within the sample. First, spherical aluminum oxide particles are measured and sorted according to the defect size desired in the reference sample. Then the sample (8620 steel powder) is consolidated in various stages using spark plasma sintering (SPS) to allow for defect placement. Finally, the part is characterized ultrasonically to ensure densification, and to verify defect location. Because SPS operates by applying simultaneous current and pressure to the part, densification can be achieved quickly, while the microstructure remains homogeneous [22]. A flat edge is then machined on the reference sample.

To determine the optimum angle of incidence for inspection at each frequency using spherically focused transducers (focal length in water of 50 mm for 7.5 and 10 MHz; 75 mm for 15 MHz; each has an element diameter of 12.5 mm). The reflection from the flat edge is used to perform an angle calibration. The calibration setup is shown schematically in FIG. 3.

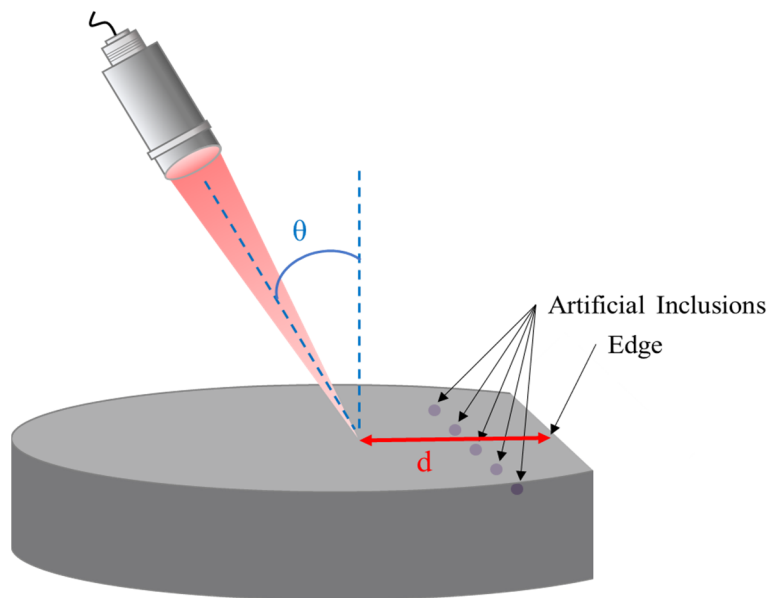


FIG. 3- Schematic showing the reference sample and surface wave angle calibration setup, in which θ is the angle of incidence and d is the distance to the edge.

For the angle calibration setup, the sample is placed so that the selected surface was normal to the transducer beam at longitudinal incidence. Then, the transducer is rotated through angles of incidence varying from 26-34 °, at 0.5 ° increments. For the measurements at each angle, the distance d , as shown in FIG. 3, is kept constant. The angle at which the maximum edge reflection amplitude occurs is selected as the inspection angle for any further measurements conducted at the given frequency. The selected values for inspection angles are given in Table 2.

Table 2. Angles selected for each frequency based on angle calibration measurements.

Frequency [MHz]	Angle [°]
7.5	31.5
10	30.5
15	30.5

To determine the gate parameters, the amplitude ratio between the known defect reflection and the reflection of the machined edge is used. To calculate this ratio, the A-scan collected for each frequency must include both reflections and neither reflection must be saturated. Multi-frequency surface wave scans are conducted on the reference sample. The location providing the maximum unsaturated reflection amplitude from both the edge and the synthetic inclusion is considered in each case.

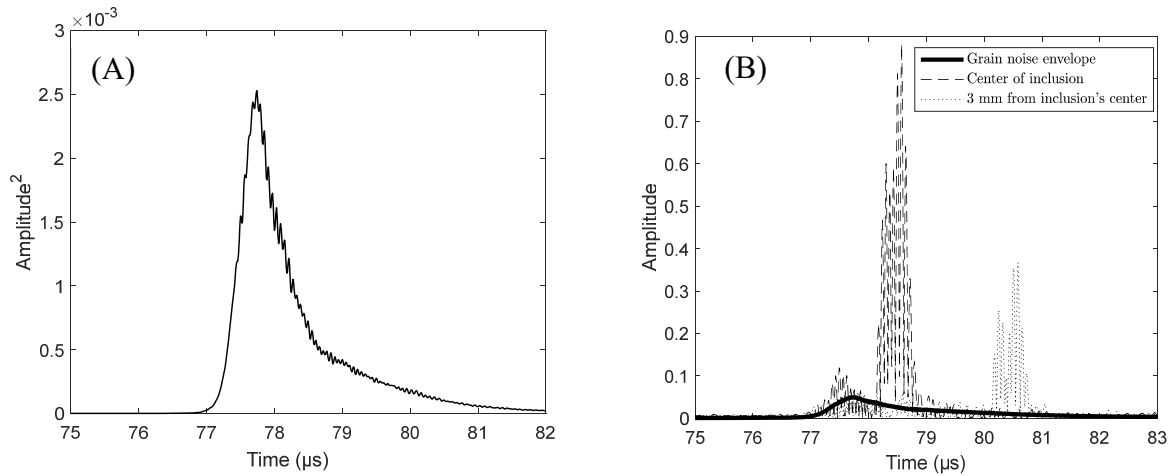


FIG. 4- Images showing the (A) variance of grain noise at 55 dB for a 7.5 MHz surface wave and (B) comparison of grain noise to a reflection from an inclusion (signal to noise) at two different locations.

The level of grain noise plays an important role in the detectability of an inclusion. For this reason, the grain noise is quantified for three different frequencies (7.5, 10 and 15 MHz). The information from the grain noise is used to identify the location of the gate and the minimum expected level of the reflection amplitude for detection of an inclusion. FIG. 4 shows an example of the grain noise and the change of the reflection amplitude from an inclusion as a function of time. A higher value of the signal-to-noise ratio for an inclusion is beneficial for detection of inclusions with greater certainty. The reflection amplitudes from all inclusions located at different depths of the reference sample are collected and the resulting amplitude ratios of the synthetic defects to the edge are plotted in a two-dimensional contour plot as shown in FIG. 5. The contour plots show the behavior

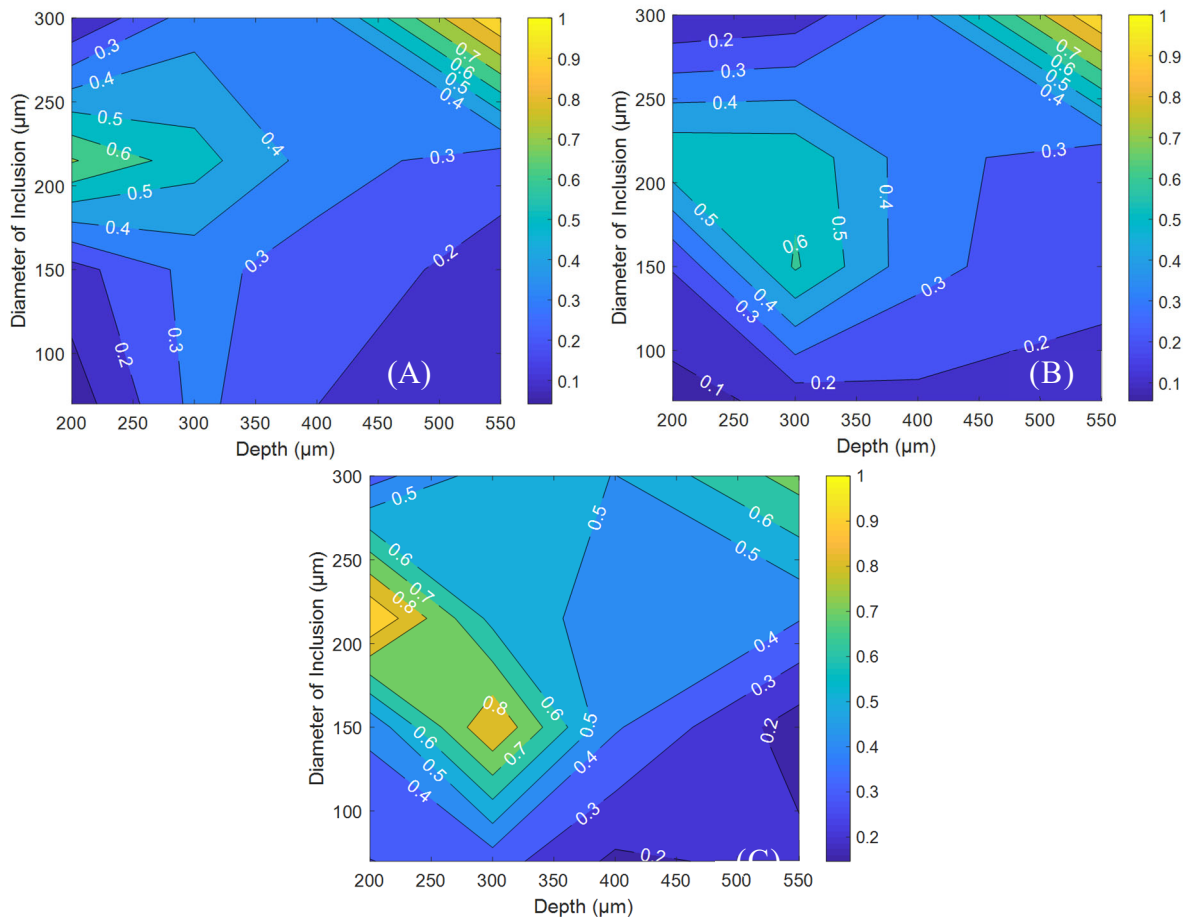


FIG. 5- Contour plots generated from the ratio of experimental inclusion reflection to edge reflection amplitudes at four different depths from the top of the reference sample for four different inclusion sizes: (A), (B) and (C) show this ratio at 7.5, 10, and 15 MHz, respectively.

of the normalized reflection amplitude for inclusions of various sizes and depths. Two locations of maximum amplitude are observed in all cases: at the shallowest depths and at the deepest location investigated. The former can be fully attributed to the amplitude of the surface wave, while the latter is likely the results of shear waves that reflect from the deeper inclusions. Although a combination of surface and shear wave detection is possible from this surface wave experimental setup, further exploration of this effect is outside the scope of this work.

Effect of Part Curvature and Associated Corrections

In order to set the gate threshold for bearing components to be scanned, some corrections are necessary due to inherent differences between the reference sample and each component. Bearing raceways are curved and this curvature impacts the amount of energy imparted to the sample by the transducer. FIG. 6 shows schematically the difference in spot size for samples with three different curvatures. To compare the effect of curvature from one sample to another, waveforms are collected at different gains at a fixed distance in time for three different frequencies (7.5, 10 and 15 MHz). FIG. 7 shows the different races, curvature, and location in time of the collected edge reflection amplitude. The edge reflection amplitude is shown as a function of the corresponding amplifier gain (FIG. 8). From these plots, it is clear that the gain characteristics depend on the curvature of the surface. For a given transducer position, the spot size of the incident

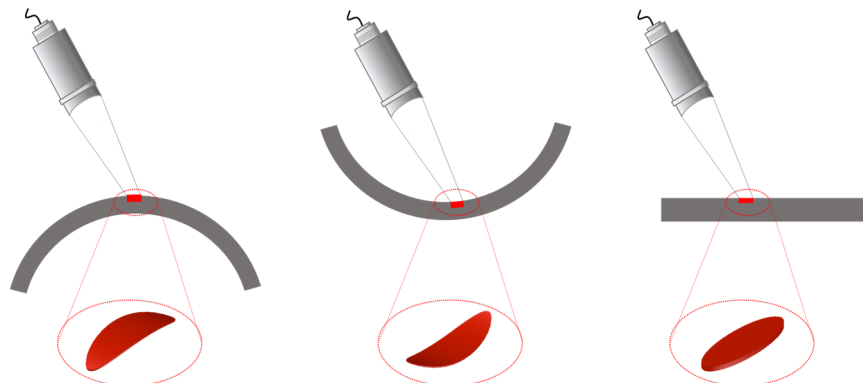


FIG. 6- Schematic showing the difference in curvature for an inner ring, an outer ring, and the flat reference sample.

energy is different. In order to normalize measurements to a single baseline, we can correct for the gain and shift the curves in FIG. 8 to a single curve. Using the results from the reference sample as a baseline, we computed a gain adjustment factor for all frequencies of interest. These gain adjustment factors are shown in Table 3. The shifted results are shown in FIG. 8 to confirm that the shifts are correct.

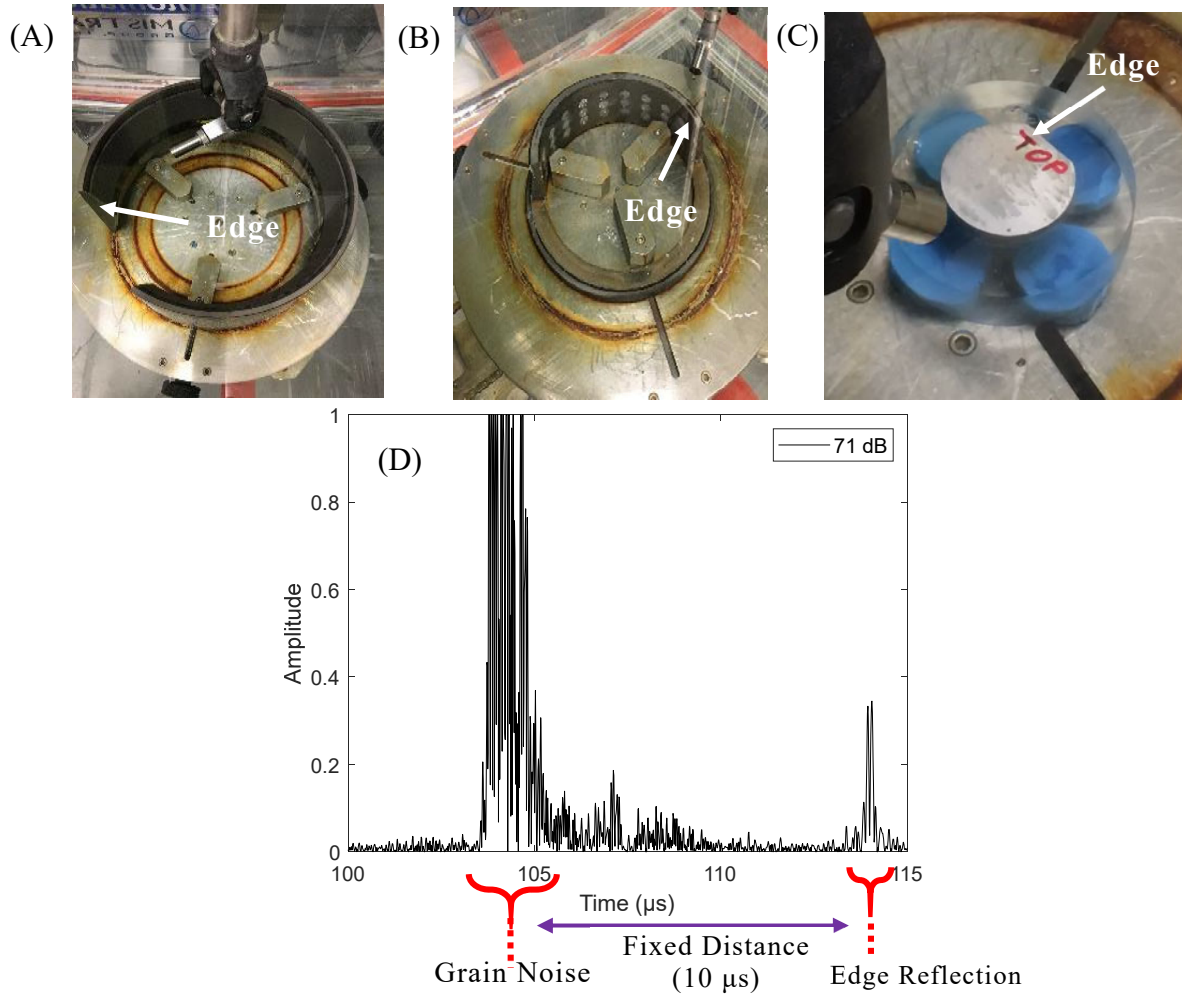


FIG. 7-Figures (A), (B) and (C) show the edge and curvature of a bearing concave, convex and flat geometry, respectively. Figure (D) shows an example rectified waveform in which the grain noise (saturated for this amplifier gain) and the edge reflection are

Table 3. The required shifts (dB) for the curvature correction for each frequency.

Part Name	15 MHz	10 MHz	7.5 MHz
Inner ring	-5	+6.3	+3.5
Outer ring	-9	-8.2	-5
Reference Sample	0	0	0

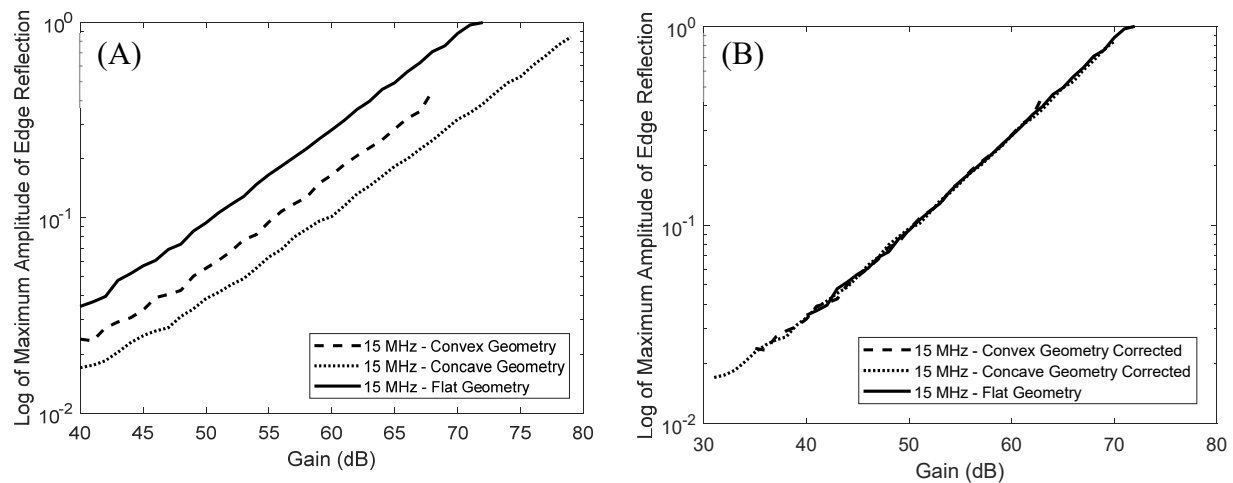


FIG. 8- Curves showing the difference in reflection amplitude for all three frequencies among three different parts. Figure (A) shows the difference in reflection amplitude due to curvature for a frequency of 15 MHz and (B) shows that the curves coincide once they are shifted onto a reference.

Finite Element Modeling

Identification of critical inclusion depth and size is vital for bearing performance and successful implementation of subsurface scanning. To be precise, the increase in subsurface stress induced by the inclusion is of great importance. The larger the increase in stress, the more likely it is that the inclusion will initiate a crack. The role of inclusion size and depth on the resulting stress surrounding an inclusion was studied using the finite element (FE) method. For this purpose, the software ANSYS was used by importing known bearing geometries and prescribing loads. An initial model without an inclusion was solved first providing baseline information. The initial

model was created based on the finite element model of Mason [23] in which the details of the boundary conditions are provided. This model has three bodies: outer ring, roller, and inner ring. The load path travels from the outer ring through the roller and into the inner ring. A representative mesh is shown in FIG. 9.

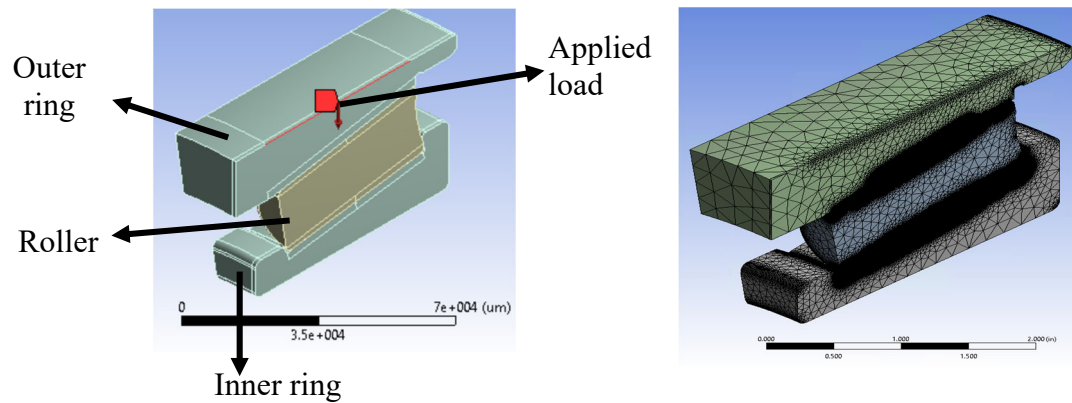


FIG. 9-ANSYS model of the 10 ° section of the bearing. The image on the right shows the denser mesh around the contact region.

By applying a dense mesh around the areas of contact between bodies, an accurate calculation of the stress is obtained. To double check the accuracy, an even finer mesh is applied to the model and the results are compared. If the results of both models are within 5-10% of each other, the model has achieved mesh independency. This outcome implies that the applied mesh does not grossly affect the results of the model.

Next, a sub-model was created using only the inner ring and the inclusion. The sub-model consists of an alumina inclusion (elastic modulus, $E = 375$ GPa) within a steel matrix ($E = 200$ GPa). By taking the contact pressure between the roller and inner ring from the initial model and applying it in the sub-model, the resulting model size is greatly reduced. This procedure also allows a finer mesh to be used around the inclusion taking solve time into consideration. FIG. 10 shows the location of the inclusion within the finite element model.

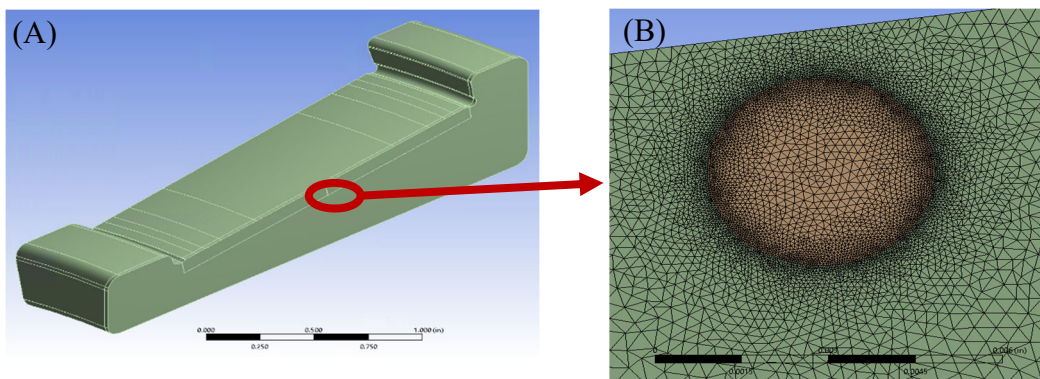


FIG. 10- Finite element details: (A) shows the meshed model of the inner ring. (B) shows the zoomed in view of the inner ring where spherical alumina inclusions are placed.

The depth and size of the inclusion are varied to generate a dataset of stresses. FIG. 11 shows the path and the resulting contour plot of maximum subsurface von Mises stress on the inner ring for inclusions of different size and depth.

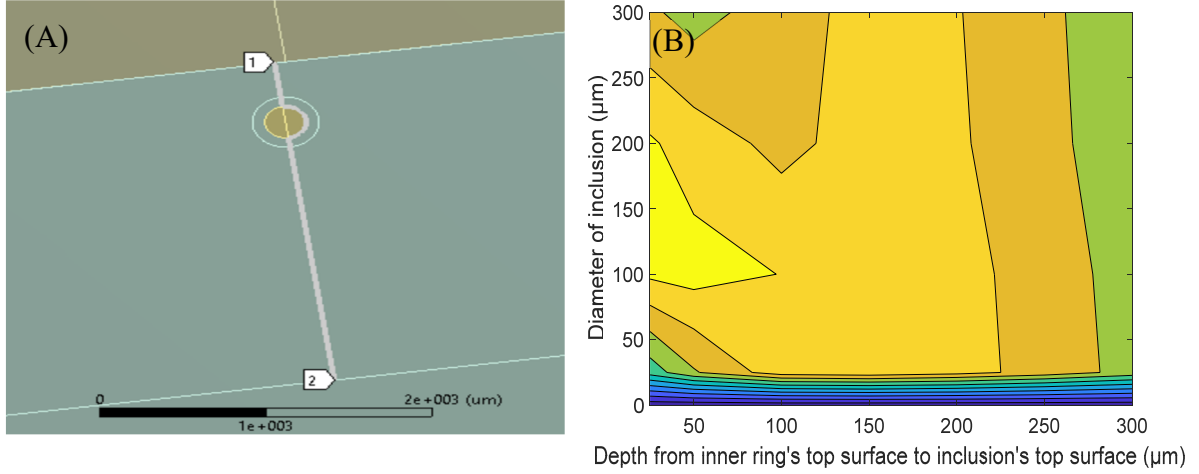


FIG. 11- Finite element model and results: (A) stress measured parallel to the applied force starting from the race surface of the inner ring (point 1 to point 2) in the steel matrix; (B) contour plot showing the variation of von Mises stress for inclusions with respect to diameter and depth.

Surface Wave Model

The study of scattering of surface waves from an elastic spherical obstacle provides information which can be used to quantify the depth and size of the subsurface inclusions. Displacements and stresses from the solution of the equations governing the Rayleigh waves are discussed in detail in Viktorov [24]. The solution given by Einspruch, et al. [25] for scattering of a shear wave can be used with the displacement expression given by Viktorov [24] as an approximation for the full solution of the scattering of a surface wave by an elastic spherical obstacle. The rate of scattered energy from a shear wave scattering by a sphere is given by [25]

$$\dot{Q}_s = \frac{i\omega}{2} \int_0^\pi \int_0^{2\pi} [(\sigma_{rr}\bar{s}_r + \sigma_{r\theta}\bar{s}_\theta + \sigma_{r\phi}\bar{s}_\phi) - (\bar{\sigma}_{rr}s_r + \bar{\sigma}_{r\theta}s_\theta + \bar{\sigma}_{r\phi}s_\phi)] a^2 d\phi \sin\theta d\theta, \quad (1)$$

where σ and s are the stress and displacement terms. The subscripts on stress and displacement denote the directions in spherical coordinates. Also, ω is the radial frequency of the wave, a is the radius of the scatterer, and the overbar on σ and s defines their complex conjugates. As the surface

wave propagates, the signal reflected from an inclusion is associated with the energy scattered in the backward direction. In this case, Eq. 1 can be simplified as

$$\dot{Q}_{bw} = \frac{i\omega}{I_{bw}}, \quad (2)$$

where

$$I_{b\omega} = (\sigma_{rr}\bar{s}_r + \sigma_{r\theta}\bar{s}_\theta + \sigma_{r\phi}\bar{s}_\phi) - (\bar{\sigma}_{rr}s_r + \bar{\sigma}_{r\theta}s_\theta + \bar{\sigma}_{r\phi}s_\phi). \quad (3)$$

The rate of energy scattering in the backward direction from a spherical obstacle can be found from Eq. 2. Because this rate is known for spherical obstacles, the size and depth of an inclusion can be quantified by comparing the theoretical model with the experimental values.

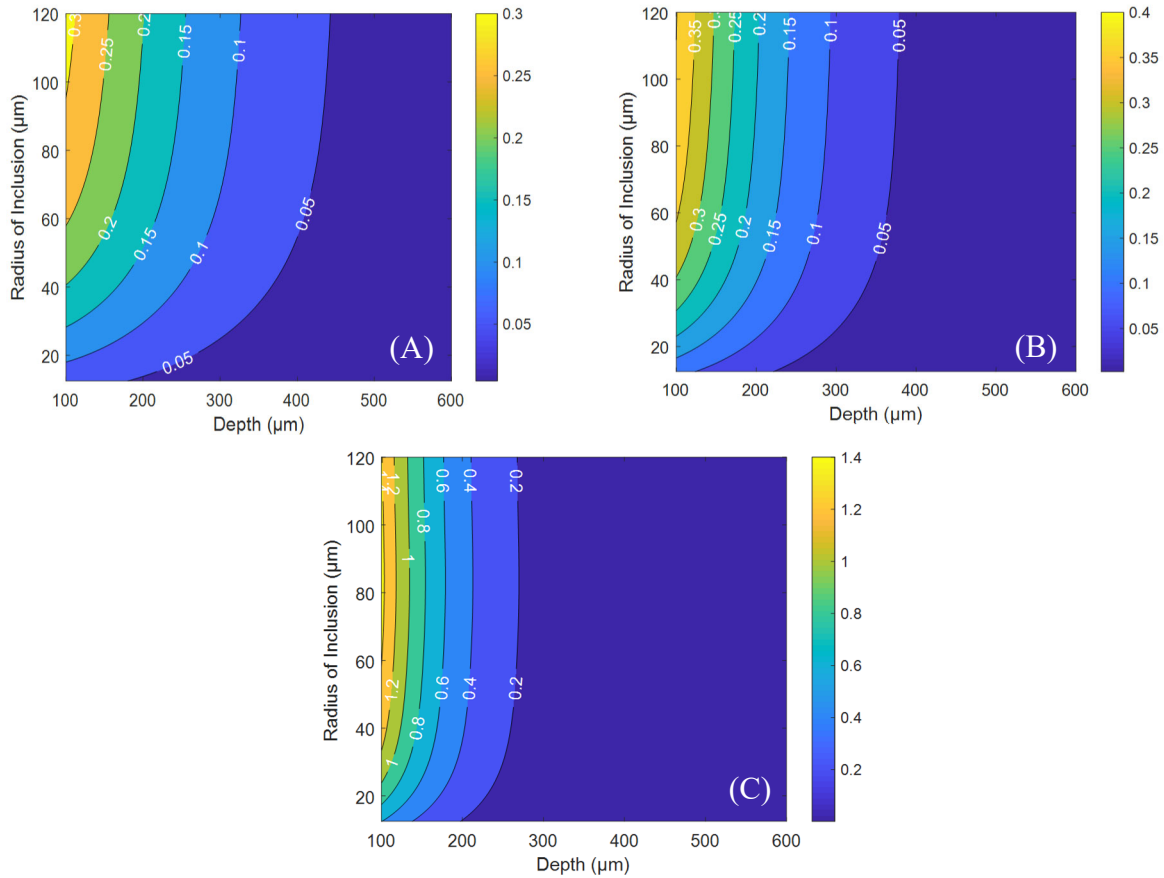


FIG. 12- Contour plot generated using the surface wave model for the ratio of the inclusion reflection to edge reflection amplitude. (A), (B) and (C) show this ratio for a surface wave of 7.5, 10 and 15 MHz, respectively.

For the inclusions shown in FIG. 2, the ratio of the inclusion reflection amplitude to the edge reflection amplitude for a surface wave of 7.5, 10 and 15 MHz are measured. These ratios are then used in the surface wave model with a tolerance of 1 %. The contour plots relating inclusion radius and depth using the surface wave model are shown in FIG. 12. Specific contours for the values measured experimentally are plotted together in FIG. 13. Ideally, the three lines should cross at a single point. However, the approximation used in the model is based on a spherical inclusion which is not necessarily applicable for all cases as exemplified by the image of the stringer shown in FIG. 2(A). Thus, more complex behavior of the curves is expected. However, the two intersection points suggest an inclusion on the order of $\sim 35 \mu\text{m}$ in radius at a depth of $\sim 400 \mu\text{m}$. Such information does provide a reasonable approximation for the inclusion, albeit within the constraints of the model. This example highlights the utility of the approach for inclusion quantification. The entire inclusion detection process described in this article is summarized in the flowchart shown in FIG. 14. The flowchart includes the steps for calibration, the stresses derived from FE analysis, the surface wave model and the details of the part to be scanned. Further studies are needed to quantify the limits of this approach and to investigate the various assumptions used for the model and measurements.

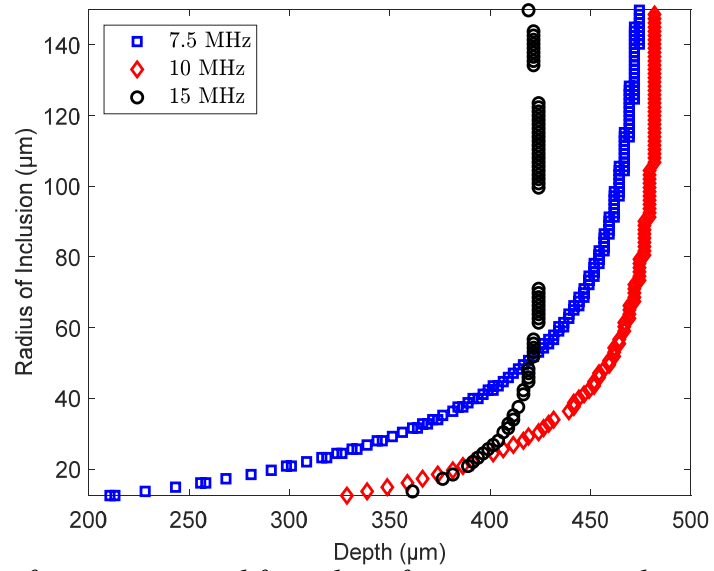


FIG. 13. Three sets of points extracted from three frequencies using the surface wave model: (A) contours based on the stringer morphology shown in FIG. 2(A).

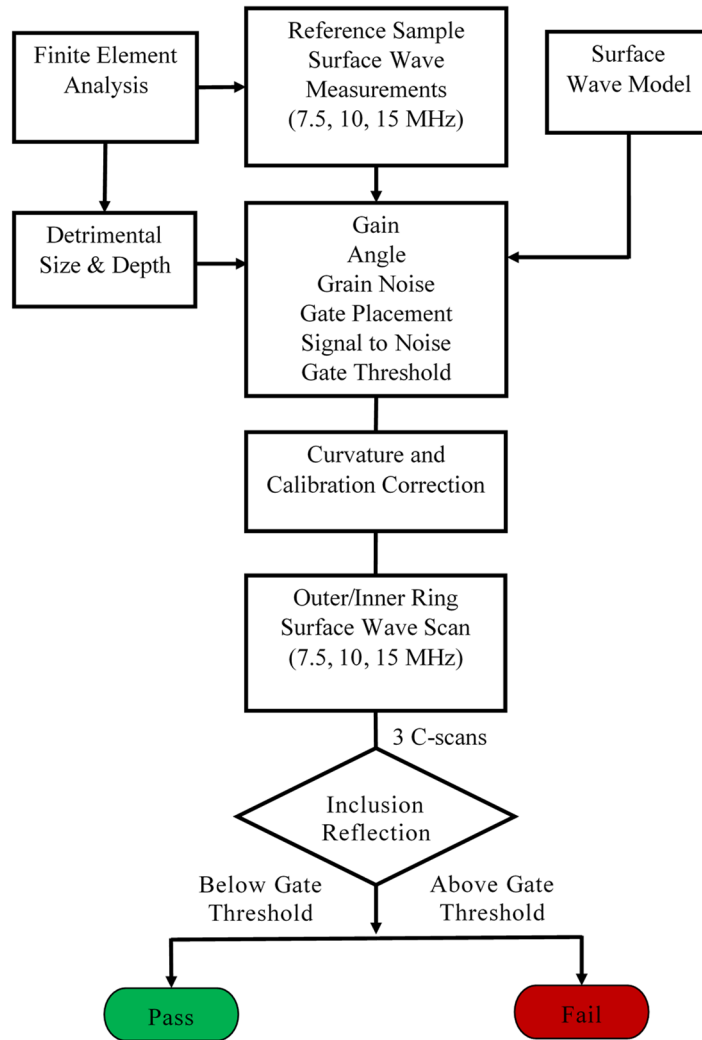


FIG. 14- Flowchart showing the components necessary for quantitative identification of subsurface inclusions.

Conclusions

In this article, a method to quantify the size and depth of subsurface inclusions has been described. This methodology is based on a reference sample with known inclusions as well as a surface wave model for spherical inclusions. The model predicts the location and depth of each inclusion. The prediction can be further studied with the help of the data collected from the reference sample. The model predicts the size of the inclusion with reasonable accuracy, but further study is required to validate the model, especially in light of the assumptions used.

References

- [1] F. Sadeghi, B. Jalalahmadi, T. S. Slack, N. Raje, and N. K. Arakere, "A Review of Rolling Contact Fatigue," *J. Tribol.*, vol. 131, no. 4, p. 041403, 2009.
- [2] T. Harris and M. Kotzalas, *Essential Concepts of Bearing Technology*, 5th ed. Boca Raton: CRC Press, 2006.
- [3] M. G. Dick and B. M. Wilson, "Roller Loads and Hertzian Contact Stress Modeling in Railcar Bearings Using Finite Element Analysis," in *Proceedings of the ASME RTD/TTCI Roller and Journal Bearing Symposium*, 2007.
- [4] T. B. Lund and K. Törresvoll, "Quantification of Large Inclusions in Bearing Steels," in *Bearing Steels: Into the 21st Century*, 1998, pp. 27–38.
- [5] H. K. D. H. Bhadeshia, "Steels for Bearings," *Prog. Mater. Sci.*, vol. 57, no. 2, pp. 268–435, 2012.
- [6] J. M. Beswick, *Bearing Steel Technology: Advances and State of the Art in Bearing Steel Quality Assurance. 7th Volume*. ASTM International, 2007.
- [7] A. Grabulov, R. Petrov, and H. W. Zandbergen, "EBSD Investigation of the Crack Initiation and TEM/FIB Analyses of the Microstructural Changes Around the Cracks Formed Under Rolling Contact Fatigue (RCF)," *Int. J. Fatigue Vol.*, vol. 32, no. 3, pp. 576–583, 2010.
- [8] A. Gupta, S. Goyal, K. A. Padmanabhan, and A. K. Singh, "Inclusions in Steel: Micro–macro Modelling Approach to Analyse the Effects of Inclusions on the Properties of Steel," *Int. J. Adv. Manuf. Technol.*, vol. 77, no. 1–4, pp. 565–572, 2015.
- [9] J. Guan, L. Wang, C. Zhang, and X. Ma, "Effects of Non-metallic Inclusions on the Crack Propagation in Bearing Steel," *Tribol. Int.*, vol. 106, pp. 123–131, 2017.
- [10] Y. Song, J. A. Turner, Z. Peng, and C. Chen, "Enhanced Ultrasonic Flaw Detection Using an Ultrahigh Gain and Time-Dependent Threshold," *IEEE Trans. Ultrason. Ferroelectr. Freq. Control*, vol. 65, no. 7, pp. 1214–1225, 2018.
- [11] Y. Song, C. M. Kube, Z. Peng, J. A. Turner, and X. Li, "Flaw Detection With Ultrasonic Backscatter Signal Envelopes," *J. Acoust. Soc. Am.*, vol. 145, no. 2, pp. EL142–EL148, 2019.
- [12] Y. Fu, P. Hu, J. A. Turner, Y. Song, and X. Li, "Ultrasonic Flaw Detection for Two-Phase Ti-6Al-4V Based on Secondary Scattering," *NDT E Int.*, vol. 102, pp. 199–206, 2019.
- [13] Y. Huang, J. A. Turner, Y. Song, P. Ni, and X. Li, "Enhanced ultrasonic detection of near-surface flaws using transverse-wave backscatter," *Ultrasonics*, vol. 98, pp. 20–27, 2019.
- [14] EN 12080 Annex A, "Railway Applications—Axleboxes—Rolling Bearings," in *European Committee for Standardization*, 2010.
- [15] D. Chen, H. Xiao, and J. Xu, "An Improved Richardson-Lucy Iterative Algorithm for C-scan Image Restoration and Inclusion Size Measurement," *Ultrasonics*, vol. 91, pp. 103–113, 2019.
- [16] L. W. Koester, C. Zuhlke, D. Alexander, A. J. Fuller, and J. A. Turner, "Near-Race Ultrasonic Detection of Subsurface Defects in Bearing Rings," in *Bearing Steel Technologies: 9th volume, Advances in Rolling Contact Fatigue Strength Testing and Related Substitute Technologies*, 2012, pp. 84–101.
- [17] C. Tarawneh, L. W. Koester, A. Fuller, B. Wilson, and J. Turner, "Service Life Testing of Components With Defects in the Rolling Contact Fatigue Zone," in *Bearing Steel Technologies: 9th Volume, Advances in Rolling Contact Fatigue Strength Testing and Related Substitute Technologies*, 2012, pp. 67–83.

- [18] P. B. Nagy and J. H. Rose, “Surface Roughness and the Ultrasonic Detection of Subsurface Scatterers,” *J. Appl. Phys.*, vol. 73, no. 2, pp. 566–580, 1993.
- [19] S. I. Rokhlin and J. Y. Kim, “In Situ Ultrasonic Monitoring of Surface Fatigue Crack Initiation and Growth From Surface Cavity,” *Int. J. Fatigue*, vol. 25, no. 1, pp. 41–49, 2003.
- [20] J. Rose, *Ultrasonic Waves in Solid Media*. Cambridge: Cambridge University Press, 2004.
- [21] J. Rose, *Ultrasonic Guided Waves in Solid Media*. Cambridge: Cambridge University Press, 2014.
- [22] S. Decker, S. Martin, and L. Krüger, “Influence of Powder Particle Size on the Compaction Behavior and Mechanical Properties of a High-Alloy Austenitic CrMnNi TRIP Steel During Spark Plasma Sintering,” *Metall. Mater. Trans. A*, vol. 47, no. 1, pp. 170–177, 2016.
- [23] M. A. Mason, “A Practical Tool for the Determination of Surface Stresses in Railroad Bearings With Different Contact Geometries and Load Conditions Using Finite Element Analysis,” Virginia Commonwealth University, 2014.
- [24] I.A. Viktorov, “Rayleigh and Lamb waves: Physical Theory and Applications,” *Plenum*, no. Chapter II, 1967.
- [25] N. G. Einspruch, E. J. Witterholt, and R. Truell, “Scattering of a Plane Transverse Wave by a Spherical Obstacle in an Elastic Medium,” *J. Appl. Phys.*, vol. 31, no. 5, pp. 806–818, 1960.